Vehicle Subframe Effects on Frontal Collision

Mahtab Limouei, Shahin Hasani and Javad Marzbanrad

Iran University of Science and Technology, School of Automotive Engineering, Tehran, Iran.
E-mail: marzban@iust.ac.ir

(Received 27 April 2024; accepted 10 October 2024)

Ensuring passenger safety is a crucial consideration in designing vehicles. Forces that are transmitted to the passenger compartment, particularly during collisions, can jeopardize the safety of the passengers. Hence, minimizing forces in the vehicle body and chassis plays a crucial role in enhancing passenger safety. Many vehicles with a unibody chassis feature a subframe as a supplementary element. The primary contribution of the subframes to the performance of the vehicle is the reduction of noise and vibration. However, subframes can also improve factors such as suspension stiffness, vehicle handling, and vehicle stability. This paper examines the effect of the presence and design modifications to the subframe on vehicle body forces. To achieve this, five subframe designs with different dimensions and materials are modeled. They are then installed on a full-scale vehicle model, and frontal collisions with a barrier and a pole are simulated. The vehicle body forces during various cases of frontal collisions are studied by measuring the acceleration and acceleration magnitude of three points on the B-pillar in the time domain and frequency domains. The results indicate that a subframe can reduce vehicle body forces, with the subframe's design influencing the extent of this effect.

1. INTRODUCTION

Passenger safety is an essential aspect of vehicle design. The subframe, as part of the suspension, can reduce vehicle forces and insulate the cabin, the passengers, the pedals, and the floor beneath the driver's feet. This leads to enhanced safety and vehicle performance.[1,2] The performance of the subframe is affected by factors such as its shape, material, cross section, manufacturing process, etc., and by paying attention to these factors, the desired performance can be achieved.[3–6] The subframe prevents the transmission of road-generated noise directly to the body and lateral components. The subframe also prevents the longitudinal components from bending. It also increases the stiffness of the engine's control arms and suspension.[7,8] The subframe is positioned near the ground and is subjected to high mechanical pressures and vibrations transmitted by the engine. The size of the subframe is dependent on the vehicle and engine.[9,10]

A vehicle can have a subframe in the front, the rear, or both the front and rear. Front subframes, also known as engine cradles, can affect the frontal collision response stiffness of a vehicle. For instance, in vehicles with longitudinal engines and rear-wheel drive, the subframe is installed in front to strengthen the suspension. In sedans, however, the subframe is positioned in the rear.[11–14] Steel, aluminum, and carbon fiber are the most used materials in subframe construction. A subframe is typically composed of compressed panels with a thickness that is significantly greater than that of body frames. Typically, subframes are attached to the body using nuts and screws.[15,16] Depending on its shape, the subframe can be utilized for various applications and purposes. Rectangular subframes, horseshoe-shaped subframes, beam cross member subframes, and butterfly subframes are currently used in a variety of vehicle designs.[14]

Front-wheel-drive vehicles with transverse engines typically have rectangular subframes. The rectangular subframe distributes the weight of the powertrain and transmission units. It also distributes the forces of these two units' dynamic reactions. In addition, it can make two independent halves of a vehicle's suspension more rigid in torsion without much assistance from the main body structure.[17,19] The horseshoe shaped subframe is used in front wheel drive vehicles with longitudinal engines. Since in these types of vehicles, the weight is concentrated in the front, a horseshoe shaped subframe, due to its shape, can provide support for the side members that are longitudinal. This configuration can also act as a platform for the lower part of the vehicle suspension, for instance, the swing arm and the anti-roll bar.[14]

Beam cross member subframes are commonly utilized in vehicles with longitudinal engines and rear wheel drive. The subframe beam cross member supports and increases the stiffness of the transverse suspension arms. The independent rear suspension of sedans is also equipped with the beam cross member subframe because the amount of support required by this suspension is comparably higher than other types of suspensions. The rear beam cross member subframe provides pivot points for the semi-trailing arms.[14] The butterfly subframe is a more modern, advantageous design. The butterfly subframe enhances the vehicle's NVH performance by reducing vibrations and decoupling the vehicle's vibration modes. By installing this type of subframe, the suspension A-arm will be replaced by two arms on each side, and the anti-roll bar will be moved from the front to the rear of the subframe, thereby

Table 1. Number of parts, elements, and nodes in the FE model.[19]

Parameter	Number
Total number of parts	510
Total number of nodes	344724
Total number of elements	333455
Solid elements	6253
Beam elements	35
Springs	4
Shell elements	327163

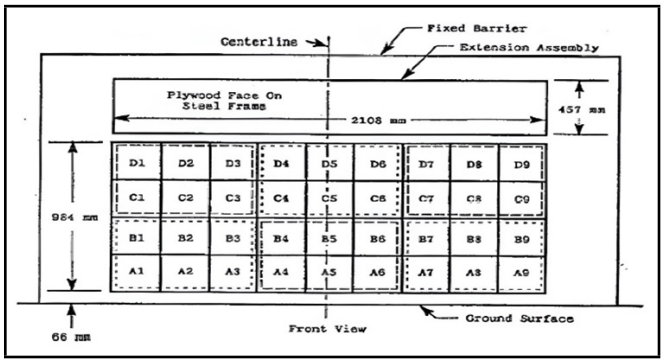

Figure 1. 36 Load cell frontal barrier designed by NCAP, front view.[19]

Table 2. Properties of the FE Model and the Test vehicle.[19]

Property	FE Model	Test Vehicle
Weight (kg)	2043	2003
Engine Type	3.8L V6	3.3L V6
Tire Size	P215/65 R15	P215/65 R15
Height—Front (mm)	798	796
Height—Rear (mm)	846	766
Wheelbase (mm)	3030	3030
Distance between the center of gravity (CG) and the front wheels centerline (CL)	1320	1319

enhancing the kinetic performance of the suspension and increasing the front axle's rolling resistance. The increase in the front axle's rolling resistance increases the vehicle's stability during high acceleration turns.[14] The present study examined the performance of five different butterfly subframe designs in two frontal collision scenarios to analyze the impact of subframe presence, dimensions, and material.

2. METHODS AND MODELLING

The National Crash Analysis Center (NCAC) of the United States created and validated the 1997 Dodge Grand Caravan finite element model in LS-DYNA software that is used in simulations and collision tests.[19] The number of parts, elements, and nodes in the finite element model is depicted in Table 1.

The NCAP (New Car Assessment Program) designed a frontal barrier comprised of six groups of six load cells (i.e., 36 load cells in total) in LS-DYNA software for collision tests. The front view of the barrier is depicted in Fig. 1.

Experimental and simulated frontal collision tests were conducted by the NCAP. The properties of the Test Vehicle and the FE Model are listed in Table 2.[19]

2.1. Collision Modeling

Simulations of frontal collisions utilized the previously described FE model (Table 2). Material Number 024, piecewise-linear-plasticity, a frequently used material in the LS DYNA software, was used to describe the material behavior of the vehicle model. The inputs needed to define the material were density, Young's modulus, poison's ratio, and yield stress. The rigid barrier was 984 by 2108 mm and was comprised of 36 load cells. The pole was 1.2 meters high, and its diameter was 0.1 m. The collisions occurred at a speed of 2.56 km/h and a zero-degree angle, and the collision offset was also zero. The road was assumed to be dry, and the temperature was 21°C.

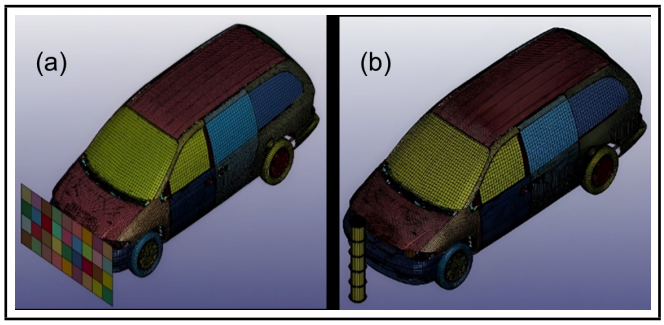

Figure 2. Frontal collision simulation: (a) rigid barrier, (b) pole.

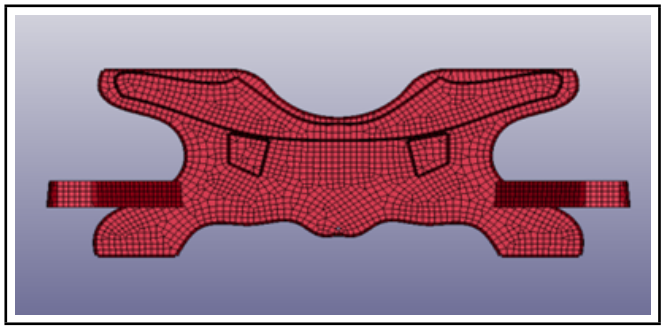

Figure 3. First subframe design.

Figure 2 depicts the simulation of the two frontal collision scenarios in the LS DYNA software.

2.2. Subframe Modeling

The butterfly subframe design was based on a reference model downloaded from the GRABCAD website. To investigate the effect of changes in the design and material of the subframe on frontal collisions, five distinct designs with varying material and geometrical properties were prepared and inserted into the 3D model of the test vehicle using the merge tool in the LS DYNA software. Detailed descriptions of these five designs are provided below:

First design: The first subframe design shared the same geometrical properties as the reference model. The design's overall dimensions were 431.386 mm in length and 964.367 mm in width. Its central region measured 267.813 mm in length and 614.719 mm in width. The design's thickness was 55.004 mm. The lateral control arms measured 63.021 mm in length and 73.208 mm in thickness. The first subframe design created in the LS DYNA software is shown in Fig. 3.

The steel alloy was chosen as the material for the first design. The material properties of the alloy are listed in Table 3.

Second design: The second design shared the same geometrical properties as the first. However, the material of choice was 6000 series aluminum alloy. The alloy's material properties are listed in Table 4.

Third design: The third design was similar in size to the first two designs overall. However, the design's thickness had decreased to 47.177 mm, and the length and thickness of the design's lateral control arms were, respectively, 63.021 and

Table 3. Material properties of the first subframe design.

Property	Value
Density (g/cm^3)	7.83
Young's modulus (GPa)	207
Poisson's ratio	0.3
Yield Stress (MPa)	363

Table 4. Material properties of the second design.

Property	Value
Density (g/cm^3)	2.7
Young's modulus (GPa)	70
Poisson's ratio	0.35
Yield Stress (MPa)	230

Table 5. Material properties of aluminum 5456-H116.

Property	Value
Density (g/cm^3)	2.63
Young's modulus (GPa)	72
Poisson's ratio	0.35
Yield Stress (MPa)	240

63.208 mm. The material of choice for the design was the same as the second design (Table 4).

Fourth design: The overall length and width of the fourth design were 431.386 mm and 964.367 mm, while the length and width of its central section were 267.813 mm and 614.719 mm. 62.084 mm was the design's thickness. The length and width of the design's lateral control arms were 63.021 mm and 80.225 mm, respectively. Since previous research has demonstrated that aluminum alloys from the 6000 series were the superior choice for sub-frame material, the same material was used in this design as in the two previous designs; only the thicknesses were altered to examine the effect of thickness.[19]

Fifth design: The design's overall length and width were 431/386 and 964/367 millimeters, while the length and width of its central section were 267/813 and 614/719 millimeters, respectively. In addition, the design had the same thickness as the fourth design, 62.084 millimeters, and the length and thickness of the lateral control arms were 63.021 millimeters and 80.225 millimeters, respectively. This design's sole purpose was to investigate the difference in performance between alloys of series 5000 and 6000. Table 5 lists the material properties of aluminum 5456-H116 used in the fifth design.

2.3. Mesh Independence Study

To investigate mesh independence and determine the optimal mesh size, six different mesh sizes were chosen for the subframe meshing. The mean of these mesh sizes was based on the mean mesh size used to model the vehicle chassis (i.e. 15 mm). These mesh sizes had been chosen: 5 mm, 7.5 mm, 10 mm, 12.5 mm, 15 mm, and 20 mm. Based on the measured tensile stress of the first subframe design along the x-axis (the vehicle's longitudinal axis), 12.5 mm appeared to be the appropriate mesh size (shown in Fig. 3), as reducing the mesh size to values less than 12.5 mm caused a difference of less than 3 percent, which was considered an acceptable error.

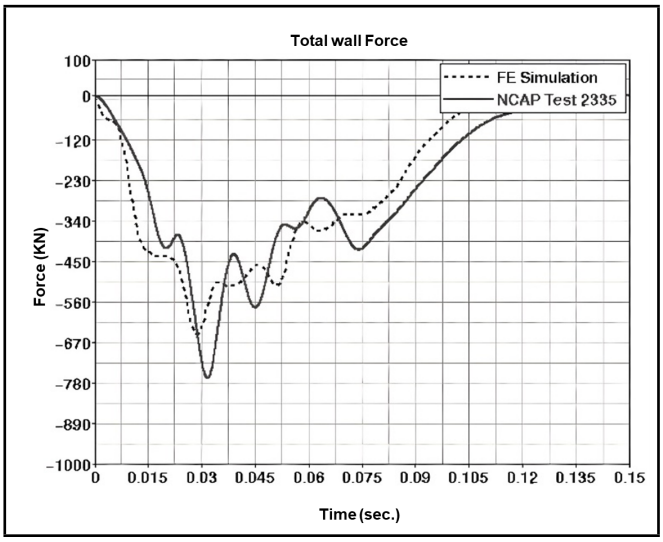

Figure 4. The applied force—simulation vs. experiment.[16]

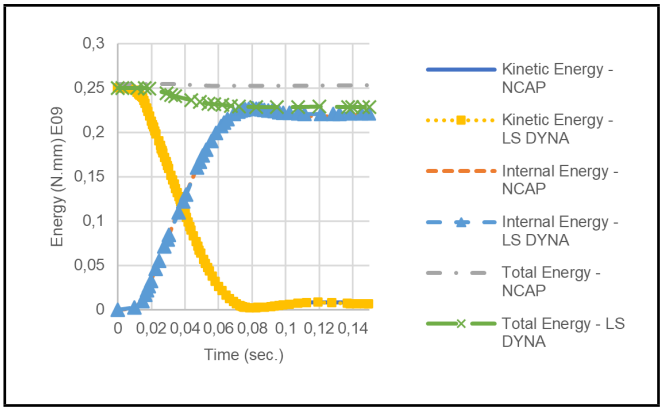

Figure 5. Energy-time curves—NCAP vs. LS DYNA.

2.4. Verification of the Vehicle Model

To confirm that the FE model of the 1997 Dodge Grand Caravan by NCAC produced the same results as the test vehicle, the applied force by the frontal rigid barrier is measured in both the simulation and the experiment. The experimental and simulated data for the applied force are displayed in Fig. 4.

Based on the results, the FE model can be regarded as an appropriate representative for the test vehicle. In addition, the energy-time curves provided by NCAP are compared with the energy-time curves obtained from the LS DYNA simulation to verify that the vehicle model used in the LS DYNA simulation produces results with acceptable accuracy. Figure 5 depicts these energy-time curves.

Comparing the energy curves by NCAP and LS DYNA simulation reveals that the model used in the current study yields the same result as the NCAP FE model, and thus the test vehicle itself. So that the results of LS DYNA simulations can be relied upon.

2.5. Verification of the Subframe Design

To validate the sub-frame design, two methods were implemented. The results of the simulations performed on the first subframe design and the reference model were compared in the first method. The second method consisted of simulating

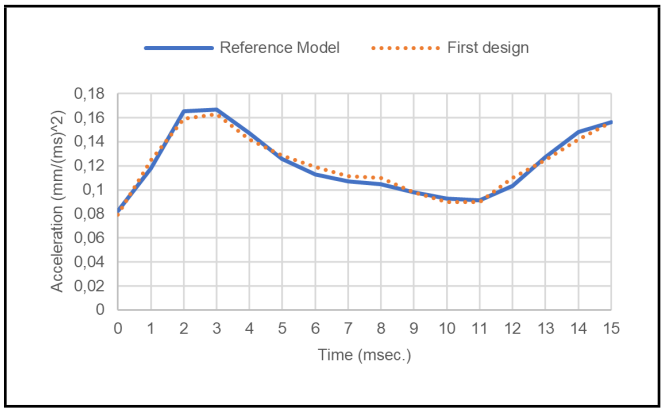

Figure 6. x-axis acceleration, reference model and first design.

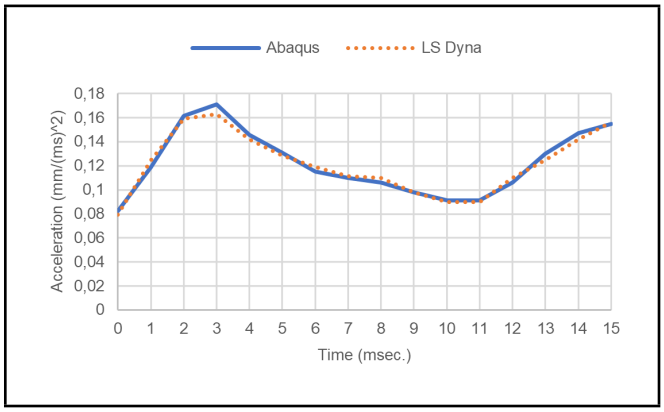

Figure 7. x-axis acceleration, Second design, Abaqus and LS DYNA.

the same conditions on the second design of the subframe in Abaqus and LS Dyna and comparing the results. The conditions of the simulation are described as follows: The lateral control arms were constrained, and a rigid wall was defined in front of the subframe, which collided with the subframe at a speed of 56 km/h. The mesh size of the subframe was defined as 12.5 mm. The material used in simulations was defined similarly to the material used to describe the vehicle model in the collision tests, and the properties of the material were in accordance with the properties listed in Table 3. Figure 6 depicts the x-axis (the vehicle's longitudinal axis) acceleration (a_x) of the reference subframe model and the first subframe design.

The difference between the results of the reference model and the first subframe design is negligible. This indicates that the subframe was correctly modeled in LS DYNA. Figure 7 shows the x-axis acceleration (a_x) for the second subframe design from Abaqus and LS DYNA simulations.

3. RESULT AND DISCUSSION

To investigate the effect of the subframe and its design on the vehicle's forces, the acceleration of the vehicle's B-pillar was measured during a frontal collision with the defined rigid barrier and pole. Three points, (a), (b), and (c), were selected on the B-pillar, and the acceleration was measured in six cases: without the subframe and with five different subframe designs. The locations of these points are depicted in Fig. 8.

Furthermore, to analyze the acceleration data in the frequency domain, the acceleration data was transformed us-

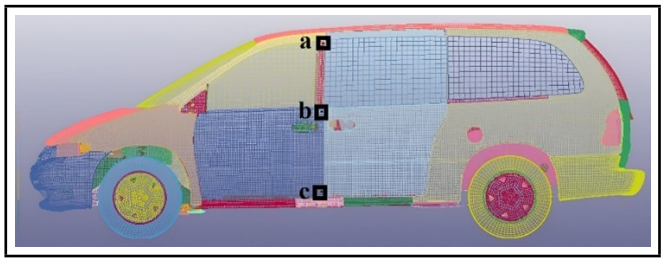

Figure 8. Selected points on the B-pillar.

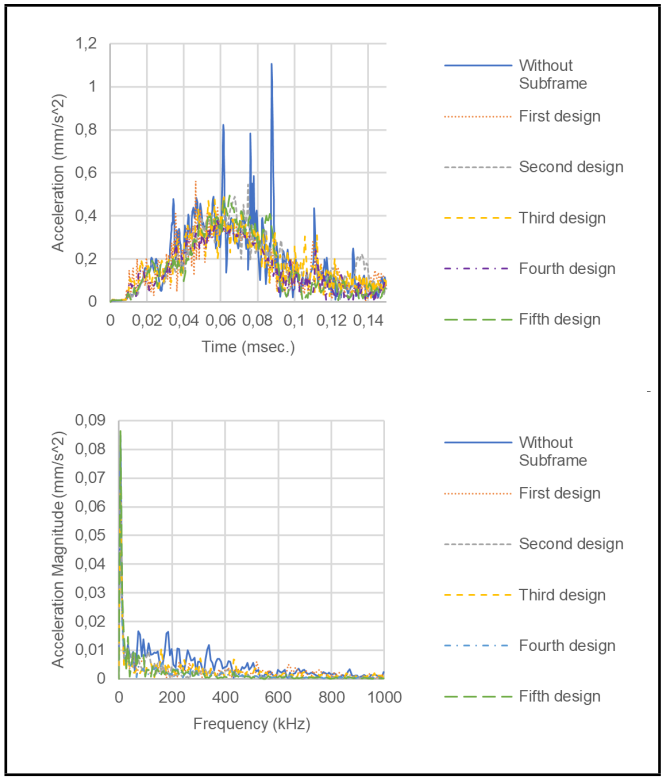

Figure 9. Rigid barrier collision at point (a), six cases (acceleration in terms of time (upper) and acceleration magnitude (lower)).

ing the fast Fourier transform in MATLAB software, and frequency-dependent graphs of the acceleration magnitude were generated. The results indicate that installing a subframe, regardless of its design, reduces overall acceleration and acceleration magnitude across all scenarios.

3.1. Rigid Barrier Collision

Figures 9–11 depict the acceleration in terms of time and the acceleration magnitude in terms of frequency at points (a), (b), and (c), respectively, for the rigid barrier collision in the six different cases.

Tables 6 and 7 illustrate the average and maximum acceleration and acceleration magnitude values, respectively, at point (a) for the rigid barrier collision, as well as the percentage difference between the average values associated with five different subframe designs and the case with no subframe installed.

The presented data indicates that at point (a) during rigid barrier collision, the first and fourth subframe designs have the highest reduction of average acceleration, respectively, while the fourth and fifth designs, respectively, have the highest reduction of average acceleration magnitude. Tables 8 and 9 de-

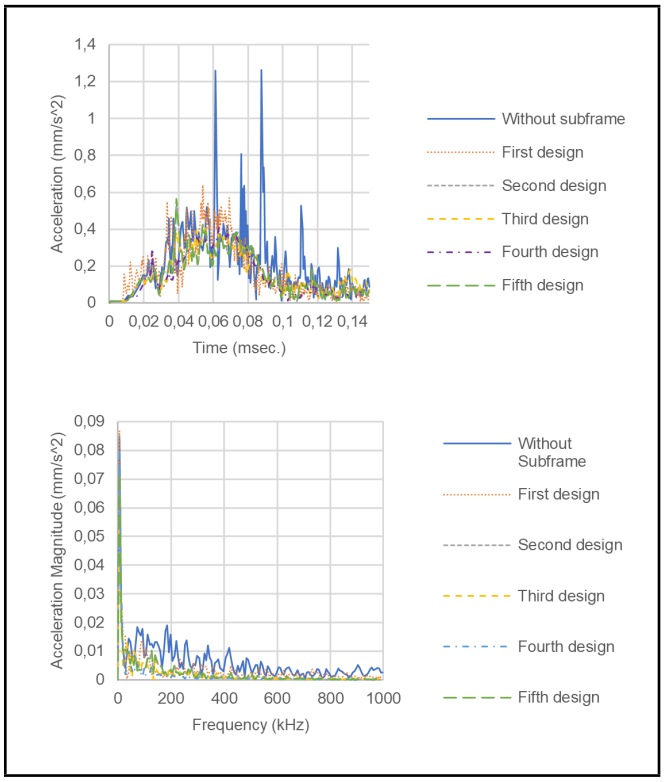

Figure 10. Rigid barrier collision at point (b), six cases (acceleration in terms of time (upper) and acceleration magnitude (lower)).

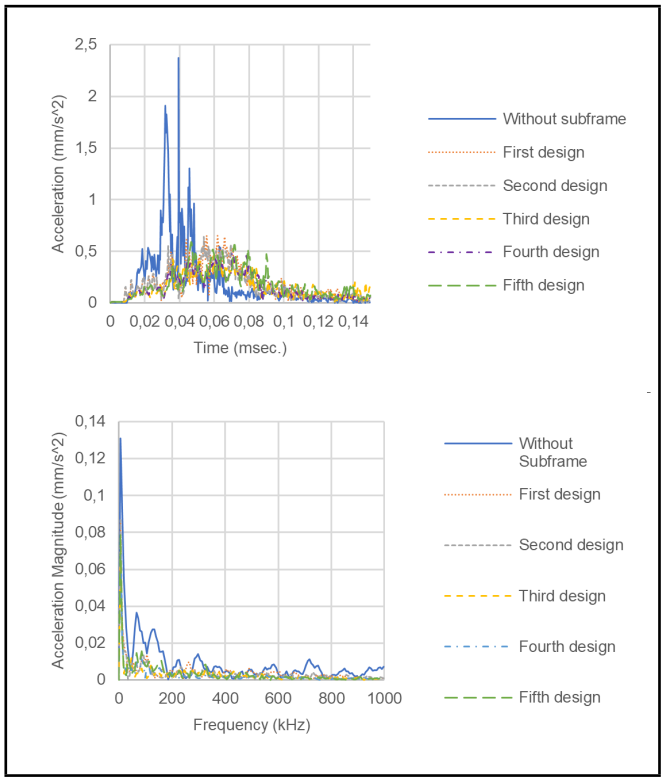

Figure 11. Rigid barrier collision at point (c), six cases (acceleration in terms of time (upper) and acceleration magnitude (lower)).

Table 6. Average and maximum acceleration at point (a)—rigid barrier collision.

Case	Max. acc. (mm/s^2)	Avg. acc. (mm/s^2)	Difference (%)
No subframe	1.10751	0.2406	–
1st design	0.562055	0.1597	-33.6093
2nd design	0.545455	0.1860	-22.6988
3rd design	0.499209	0.1935	-19.57882
4th design	0.377866	0.1645	-31.61682
5th design	0.495059	0.1892	-21.37340

Table 7. Average and maximum acceleration magnitude at point (a)-—rigid barrier collision.

Case	Max. acc. magnitude (mm/s^2)	Avg. acc. magnitude (mm/s^2)	Difference (%)
No subframe	0.084721672	0.006182875	–
1st design	0.064502856	0.003969971	-35.7909
2nd design	0.070425653	0.00360157	-41.7493
3rd design	0.068543545	0.004006423	-35.2013
4th design	0.069823683	0.003019216	-51.16809
5th design	0.086448507	0.003315173	-46.3814

Table 8. Average and maximum acceleration at point (b)—rigid barrier collision.

Case	Max. acc. (mm/s^2)	Avg. acc. (mm/s^2)	Difference (%)
No subframe	1.26166	0.2303	–
1st design	0.637747	0.1775	-22.9217
2nd design	0.564427	0.1762	-23.5021
3rd design	0.414032	0.1619	-29.7057
4th design	0.41502	0.1508	-34.5019
5th design	0.565714	0.1687	-26.7486

Table 9. Average and maximum acceleration magnitude at point (b)-—rigid barrier collision.

Case	Max. acc. magnitude (mm/s^2)	Avg. acc. magnitude (mm/s^2)	Difference (%)
No subframe	0.084836589	0.007581351	–
1st design	0.086873589	0.00468172	-38.2469
2nd design	0.072038125	0.003387742	-55.3148
3rd design	0.064570848	0.003134883	-58.6501
4th design	0.079324952	0.002698707	-64.4033
5th design	0.07183611	0.003341809	-55.9207

pict the average and maximum acceleration and acceleration magnitude values, respectively, at point (b) for the rigid barrier collision, as well as the percentage difference between the average values for five different subframe designs and the case without a subframe.

The data presented in Tables 8 and 9 indicate that at point (b), the fourth and third subframe designs, respectively, achieve the greatest reduction of the average acceleration and average acceleration magnitude during rigid barrier collision.

Tables 10 and 11 depict the average and maximum acceleration and acceleration magnitude values at point (c) for the rigid barrier collision, as well as the percentage difference between the average values for five different subframe designs and the case without a subframe.

According to the data, the third and fourth subframe designs lead to the greatest reductions in average acceleration and acceleration magnitude values during the collision with the rigid barrier at point (c).

3.2. Frontal Collision with the Pole

Figures 12–14 depict the acceleration in terms of time and the acceleration magnitude in terms of frequency at points (a), (b), and (c), respectively, for the pole collision in the six different cases.

Table 10. Average and maximum acceleration at point (c)—rigid barrier collision.

Case	Max. acc. (mm/s^2)	Avg. acc. (mm/s^2)	Difference (%)
No subframe	2.37194	0.2385	–
1st design	0.651585	0.2044	-14.2879
2nd design	0.637747	0.1809	-24.1482
3rd design	0.458105	0.1688	-29.2113
4th design	0.475771	0.1716	-28.0199
5th design	0.588142	0.1890	-20.7477

Table 11. Average and maximum acceleration magnitude at point (c)-—rigid barrier collision.

Case	Max. acc. magnitude (mm/s^2)	Avg. acc. magnitude (mm/s^2)	Difference (%)
No subframe	0.131054787	0.010307381	0
1st design	0.08635082	0.005312159	-48.4626
2nd design	0.086668351	0.004707906	-54.3249
3rd design	0.064367209	0.003860211	-62.5491
4th design	0.075154266	0.003673582	-64.3597
5th design	0.078422968	0.004523629	-56.1127

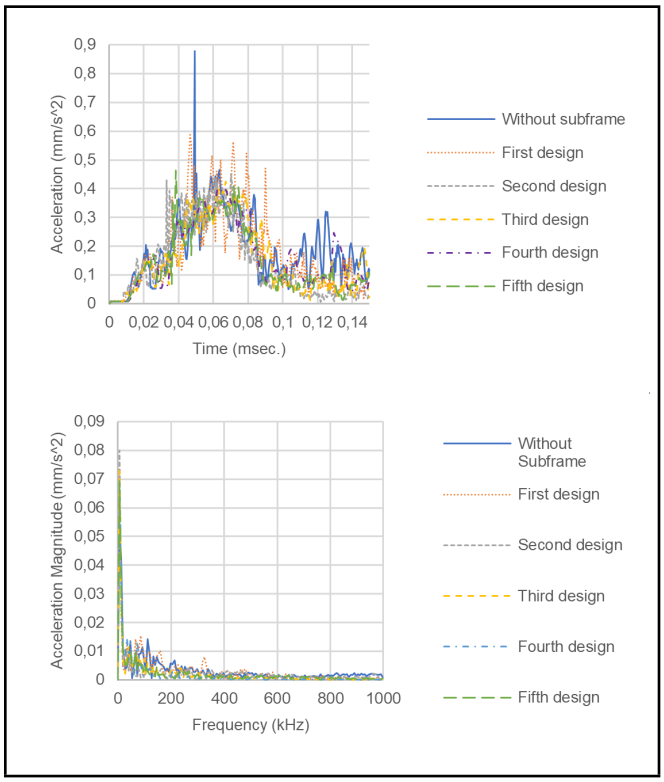

Figure 12. The pole collision at point (a), six cases (acceleration in terms of time (upper) and acceleration magnitude (lower)).

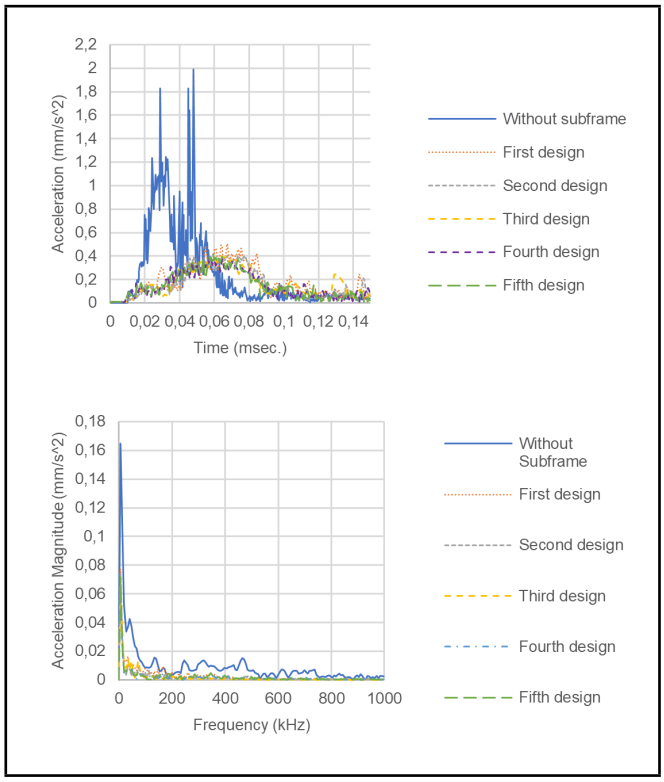

Figure 13. Collision with the pole at point (b), six cases (acceleration in terms of time (upper) and acceleration magnitude (lower)).

Table 12. Average and maximum acceleration at point (a)—rigid barrier collision.

Case	Max. acc. (mm/s^2)	Avg. acc. (mm/s^2)	Difference (%)
No subframe	0.876822	0.1970	–
1st design	0.586696	0.1753	-11.0320
2nd design	0.451581	0.1501	-23.7976
3rd design	0.423913	0.1731	-12.1315
4th design	0.403548	0.1713	-13.0718
5th design	0.462451	0.1592	-19.1961

Table 13. Average and maximum acceleration magnitude at point (a)-—rigid barrier collision.

Case	Max. acc. magnitude (mm/s^2)	Avg. acc. magnitude (mm/s^2)	Difference (%)
No subframe	0.051743754	0.004525866	–
1st design	0.078716869	0.004385161	-3.1089
2nd design	0.080054873	0.003398663	-24.9058
3rd design	0.073030324	0.003105606	-31.3809
4th design	0.063350095	0.00288079	-36.3483
5th design	0.069429455	0.003109139	-31.3029

Tables 12 and 13 depict the average and maximum acceleration and acceleration magnitude values, respectively, at point (a) for the pole collision, as well as the percentage difference between the average values for five different subframe designs and the case without a subframe.

As shown in Tables 12 and 13, the second and fifth subframe designs have the greatest reductions in average acceleration values, and the fourth and third designs cause the greatest reduction in the average acceleration magnitude at point (a) during frontal collision with the pole.

Tables 14 and 15 display the average and maximum acceleration and acceleration magnitude values at point (b) for the pole collision, in addition to the percentage difference between the average values for five different subframe designs and the case without a subframe.

As demonstrated in Tables 14 and 15, the fifth and fourth subframe designs result in the greatest reductions in average acceleration values, and the third and fourth subframe designs have the highest reduction of average acceleration magnitude, respectively, at point (b) during the pole collision.

Tables 16 and 17 present the average and maximum acceleration and acceleration magnitude values at point (c) for the pole collision, as well as the percentage difference between the average values for five distinct subframe designs and the case

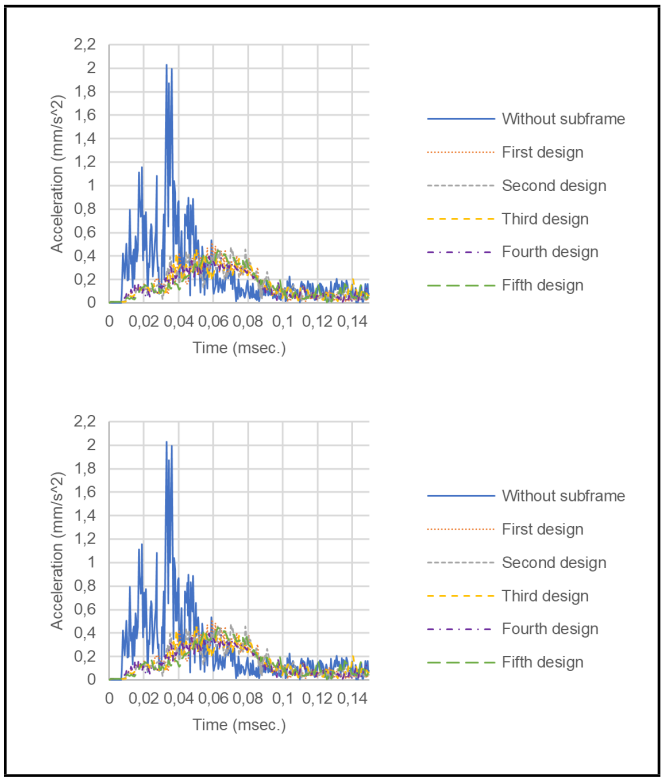

Figure 14. Collision with the pole at point (c), six cases (acceleration in terms of time (upper) and acceleration magnitude (lower)).

Table 14. Average and maximum acceleration at point (b)—rigid barrier collision.

Case	Max. acc. (mm/s^2)	Avg. acc. (mm/s^2)	Difference (%)
No subframe	1.99111	0.2462	–
1st design	0.502767	0.1672	-32.0736
2nd design	0.401186	0.1620	-34.1885
3rd design	0.40415	0.1696	-31.1057
4th design	0.396491	0.1472	-40.2104
5th design	0.421937	0.1460	-40.7042

Table 15. Average and maximum acceleration magnitude at point (b)-—rigid barrier collision.

Case	Max. acc. magnitude (mm/s^2)	Avg. acc. magnitude (mm/s^2)	Difference (%)
No subframe	0.164644097	0.010854983	–
1st design	0.077414263	0.004023111	-62.9377
2nd design	0.07403239	0.003210362	-70.425
3rd design	0.06340281	0.002891109	-73.3661
4th design	0.069018024	0.002988706	-72.465
5th design	0.071964348	0.003099745	-71.4440

without a subframe.

As shown in Tables 16 and 17, the fourth and first subframe designs result in the greatest reductions in average acceleration values, and the fourth and fifth subframe designs exhibit the greatest reduction in the average acceleration magnitude during the pole collision at point (c).

4. CONCLUSIONS

In this study, CATIA software was used to model five distinct subframe designs with different materials and geometrical properties. Five subframe designs are subsequently installed on a vehicle model in LS DYNA software, and the model is subjected to two frontal collision tests with a rigid barrier and a pole. Three points are selected on the B-pillar of the vehicle, and the acceleration and acceleration magnitude (derived from the fast Fourier transform (fft) in MATLAB software) of these points are calculated for the two collision tests in six cases: without the subframe and with the five subframe designs.

Table 16. Average and maximum acceleration at point (c)—rigid barrier collision.

Case	Max. acc. (mm/s^2)	Avg. acc. (mm/s^2)	Difference (%)
No subframe	2.02915	0.2309	–
1st design	0.51581	0.1552	-32.7894
2nd design	0.476285	0.1627	-29.5118
3rd design	0.459486	0.1589	-31.1946
4th design	0.396838	0.1538	-33.3989
5th design	0.445652	0.1651	-28.4840

Table 17. Average and maximum acceleration magnitude at point (c)-—rigid barrier collision.

Case	Max. acc. magnitude (mm/s^2)	Avg. acc. magnitude (mm/s^2)	Difference (%)
No subframe	0.133872119	0.011830216	–
1st design	0.081113942	0.003486921	-70.5253
2nd design	0.074995435	0.003673763	-68.9459
3rd design	0.067224245	0.003298746	-72.1159
4th design	0.068777551	0.003032823	-74.3638
5th design	0.074050922	0.003033487	-74.3581

The results indicate the following:

- The fourth design exhibits the most favorable overall performance in terms of decreasing the average acceleration, followed by the second and fifth designs. The gap in performance between the second and fifth designs is minimal.
- The fourth design exhibits the highest overall performance in reducing the average acceleration magnitude in terms of frequency, followed by the third and fifth designs. The disparity in performance between the third and fifth designs is small.
- The fourth design exhibits the lowest overall values for maximum acceleration, while the third and fifth designs follow suit. The difference in performance between the third and fifth designs is substantial.
- The third design exhibits the lowest overall values for maximum acceleration, followed by the fourth and fifth designs. The difference in performance between the fourth and fifth designs is significant.

Considering all factors, the fourth design is the most superior subframe in every aspect. Compared to the original design, the overall thickness and the thickness of the control arms have been increased, and the aluminum alloy 6000 series is used for this design.

REFERENCES

[1] Safaei, M., Azadi, S., Keshavarz, A., and Zahedi, M. The refinement of a vehicle NVH performance by optimizing sub-frame mounts, *SAE Technical Paper*, (2014). https://doi.org/10.4271/2014-01-1692

[2] Marzbanrad, J., Mohammadi, M., and Mostaani, S. Optimization of a passive vehicle suspension system for ride comfort enhancement with different speeds based on design of experiment method (DOE) method, *Journal of Mechanical Engineering Research*, **5** (3), 50–59, (2013). https://doi.org/10.5897/jmer10.061

[3] Angrosch, B., Plöchl, M., and Reinalter, W. Suspension design by means of numerical sensitivity analysis and optimisation, *International Journal of Vehicle Design*, **65** (1), 52–72, (2014). https://doi.org/10.1504/IJVD.2014.060065

[4] Ivarsson, L. Transfer path analysis of a vehicle subframe: Measurements in six degrees of freedom, *International Design Engineering Technical Conferences and Computers and Information in Engineering Conference*, **80401**, American Society of Mechanical Engineers, (1997). https://doi.org/10.1115/DETC97/VIB-4248

[5] Balakrishnan, P., Perumal, J., Salahudeen, A., and Kannan, J. S. Design for six sigma (DFSS) of hydroformed engine cradle design for SUV application, *SAE Technical Paper*, (2011). https://doi.org/10.4271/2011-26-0109

[6] Park, S.-Y., Park, D.-C., Yoon, K.-S., and Lee, M.-S. A study of front subframe system optimization for improving vehicle nvh performance, *SAE Technical Paper*, (2009). https://doi.org/10.4271/2009-01-2097

[7] Xu, L., Zhao, S., Xin, G., Guo, R., Song, H., and Jia, X. Research on the modeling and influence of flexible sub-frame on vehicle performance: Considering the high frequency excitation of the engine, *7th International Conference on Modeling, Simulation, and Applied Optimization (ICMSAO)*, IEEE, 1–5, (2017). https://doi.org/10.1109/icmsao.2017.7934916

[8] Wang, D. and Jiang, R. Fatigue life estimation of front subframe of a passenger car based on modal stress recovery method, *SAE International Journal of Materials and Manufacturing*, **8** (3), 795–802, (2015). https://doi.org/10.4271/2015-01-0547

[9] Li, C., Kim, I. Y., and Jeswiet, J. Conceptual and detailed design of an automotive engine cradle by using topology, shape, and size optimization, *Structural and Multidisciplinary Optimization*, **51**, 547–564, (2015). https://doi.org/10.1007/s00158-014-1151-6

[10] Shangguan, W.-B. Engine mounts and powertrain mounting systems: a review, *International Journal of Vehicle Design*, **49** (4), 237–258, (2009). https://doi.org/10.1504/ijvd.2009.024956

[11] Rotondella, V., Merulla, A., Baldini, A., and Mantovani, S. Dynamic modal correlation of an automotive rear subframe, with particular reference to the modelling of welded joints, *Advances in Acoustics and Vibration*, (2017). https://doi.org/10.1155/2017/8572674

[12] Jančář, R., Dlugoš, J., and Fridrichová, K. Influence of simplifying the geometry of the FE model of the vehicle frontal full barrier crash test, *Engineering Mechanics 2024*, 146–149, (2024). https://doi.org/10.21495/em2024-146

[13] Tampi, M. and Yang, X. Vehicle cradle durability design development, *SAE Transactions*, 1111–1119, (2005). https://doi.org/10.4271/2005-01-1003

[14] Meng, X., Sun, Y., He, J., Li, W., and Zhou, Z. Multi-objective lightweight optimization design of the aluminium alloy front subframe of a vehicle, *Metals*, **13** (4), 705, (2023). https://doi.org/10.3390/met13040705

[15] Ali, U. and Fraser, R. A. Numerical modeling of rear subframe under different loading conditions, *SAE Technical Paper*, (2013). https://doi.org/10.4271/2013-01-0571

[16] Heisler, H. *Advanced vehicle technology*, Elsevier, (2002). https://doi.org/10.1016/b978-0-7506-5131-8.x5000-3

[17] Genta, G. and Morello, L. *The Automotive Chassis. Volume 1: Components Design*, Springer Science & Business Media, (2008). https://doi.org/10.1007/978-1-4020-8676-2

[18] Weng, Y., Jin, X., Zhao, Z., and Zhang, X. Car-to-pedestrian collision reconstruction with injury as an evaluation index, *Accident Analysis & Prevention*, **42** (4), 1320–1325, (2010). https://doi.org/10.1016/j.aap.2010.02.012

[19] Chen, X., Mahmood, H., Wagner, D. A., and Baccouche, M. R. Aluminum subframe design for crash energy management, *SAE Technical Paper*, (2004). https://doi.org/10.4271/2004-01-1775